CONDENSED MATTER PHYSICS

Brownian lithographic polymers of steric lock-and-key colloidal linkages

Tianren Yu[1] and Thomas G. Mason[1,2,3]*

We design and lithographically fabricate two-dimensional preassembled colloidal linkages of custom-shaped, discrete, mobile microscale tiles that are sterically coupled together by lock-and-key sub-tile features, yielding hinge-like bonds between separate tiles. These mobile colloidal linkages, which we call polylithomers, provide top-down, preconfigured, morphologically controllable analogs of fluctuating molecular polymers. We illustrate the versatility of this approach by fabricating and studying curvilinear, branched, bridged-spiral, dendritic, and mesh-like polylithomers having controllable preassembled dimensions, topologies, configurations, intrinsic local curvatures, persistence lengths, and bond extensibilities. By advancing anisotropic particle tracking routines to handle lock-and-key tiles, we measure the dynamic conformational changes of polylithomers caused by Brownian excitations to the monomer scale, revealing markedly large bond extensibilities. Beyond modeling fluctuating semiflexible molecular polymers, polylithomers provide access to unusual polymer morphologies and bonding potentials that have not yet been synthesized through other kinds of assembly methods using either molecular or colloidal monomers.

INTRODUCTION

The compositions and structures of monomers, as well as the nature of bonds and other interactions between them, influence the resulting properties of molecular polymers. Beyond naturally occurring biopolymers, synthetic organic chemistry has provided access to an impressive array of flexible and semiflexible polymers that have different structures, shapes, functionalities, and morphologies based primarily on covalent bonds between constituent atoms through a variety of polymerization or self-assembly reactions (*1*). Examples of these include branched (*2*), star (*2*), and brush polymers (*3*), as well as larger-scale dendrimers (*2*), DNA origami (*4*), copolymers (*2*, *5*), and thermally responsive cross-linked microgel beads (*6*). In addition, remarkably, mechanically interlocked supermolecular polymer systems with complex topologies, such as smaller rings that can slide along a larger ring, have also been synthesized (*7*, *8*). While the routes of bottom-up chemical syntheses of organic molecular polymers and the control over their structures, yields, and polydispersities are continuing to advance, there are also opportunities for expanding the frontiers of polymer science through alternative routes, including those involving colloidal mimics of polymers that can be more readily visualized down to the monomer scale. These colloidal mimics enable experimental studies of polymer dynamics that can be imaged to make real-space movies using optical microscopy; this approach overcomes the limitations of imaging much smaller molecular polymers that have substantially faster dynamics by other means.

Among the first studies of colloidal mimics of polymers have been the collapse of flexible chains of fractionated microscale ferrofluid droplets initially formed by a magnetic field and held together by temperature-controlled salt-induced attractions between constituent droplet interfaces (*9*), systems of active "swimmers" that have chains of droplets bridged by flexible polymers (*10*), and self-assembled columnar chains of wax microdisks that have long persistence lengths via shape-controlled anisotropic depletion attractions (*11*, *12*) induced by nanoscale surfactant micelles. Depletion attractions have also been used to create more flexible chains of convex-concave pac-man-like particles (*13*–*15*). Other systems of colloidal mimics of polymers include chains held together by programmable interactions such as between single-stranded DNA oligomerically functionalized colloids (*16*, *17*) and size-controlled self-assembly of colloidal building blocks into various polymer architectures such as networks induced by magnetic forces (*18*). Similar colloidal systems with programmed interactions have been used to self-assemble a wide range of dense crystalline structures, too (*19*). However, none of these colloidal systems that mimic polymers have relied upon steric bonding between solid interlocking shape-designed structures that have effectively hard interactions between their surfaces. These steric bonds between colloids are unusual because no attractions and no molecular connections are used to connect the shape-complementary substructures of adjacent lock-and-key colloids. Instead, the preinserted head of one rigid lock-and-key colloid is constrained within the tail of an adjacent rigid lock-and-key colloid in a manner that sterically (i.e., geometrically) prohibits the two colloids from separating. Moreover, none of the existing self-assembly approaches offer the extremely low defect rate and high yield of the precisely desired structures in parallel as that which can be achieved through top-down lithography, particularly optical stepper lithography.

The advent of lithographically preassembled monolayers (litho-PAMs) opens up a versatile avenue for fabricating and studying new kinds of dense two-dimensional (2D) systems of shape-designed colloids that have preconfigured positions and orientations with low defects over wide areas (*20*). Until now, the litho-PAMs approach has only been used to create and study dense monolayers of microscale Penrose P2 kite and dart tiles that form a fluctuating fivefold quasi-crystal, experience Brownian excitations, and are confined within enclosing walls. This dense Penrose quasi-crystal system has been demonstrated to melt, and the tiles lose memory of their initial configuration when a wall is removed, since the in-plane interactions between the tiles are effectively hard. While studying the melting of

[1]Department of Chemistry and Biochemistry, University of California-Los Angeles, Los Angeles, CA 90095, USA. [2]Department of Physics and Astronomy, University of California-Los Angeles, Los Angeles, CA 90095, USA. [3]California NanoSystems Institute, University of California-Los Angeles, Los Angeles, CA 90095, USA.
*Corresponding author. Email: mason@chem.ucla.edu

dense systems of shape-designed hard-interacting tiles is interesting in its own right, finding a way to create long-lived many-body dynamical colloidal systems without confining walls and without inducing in-plane attractions would be highly desirable, too.

Here, we show that this desirable goal can be achieved by advancing litho-PAMs (*20*) in order to fabricate complex fluctuating colloidal chain-like lock-and-key lithographic mimics of polymers. Doing so empirically is nontrivial, since the limitations of optical diffraction must be respected and yet complete separation between all interlocking colloidal particles must be obtained robustly. By programming designer lock-and-key tile shapes and their relative positions and orientations in the lithographic mask using computer-aided design and also by optimizing lithographic production and lift-off techniques, we produce interconnected and sterically interlocked yet reconfigurable architectures of colloidal tiles that are long-lived in the absence of confining walls. Moreover, these architectures, which we call polylithomers (PLMs), are lithographically preassembled and therefore not made by resorting to programmable molecular attractions between the surfaces of the colloidal lithomer (LM) tiles. Upon release from the substrate, Brownian excitations cause these mobile PLMs to exhibit conformational fluctuations; so, entropic considerations are important just as they are for molecular polymers. These interconnected colloidal structures could be viewed from a chemical perspective as mimics of polymers that can be designed top-down to have considerable morphological complexity. Equivalently, these dynamic interconnected structures could also be viewed from a statistical mechanical perspective as Brownian systems of colloidal linkages, since linkages are mechanical assemblies composed of discrete rigid objects which have joints that couple microstates of constituent tiles.

Among models of polymers, two of the most well-known are the freely jointed chain and worm-like chain (*21*). One key assumption, common to both of these models, is that the bonds linking monomers within the polymers are inextensible. While this assumption is reasonable for most molecular polymers, in some cases under large applied force, scientists have observed (*22*, *23*) and theoretically studied (*24*) the extensibility (i.e., extensional elasticity) of polymeric bonds. Typically, it is much easier to cause a conformational change by rotating bonds that lack torsional rigidity within a molecular polymer than it is to alter the bond distance between adjacent monomers. However, so far, there is no experiment that directly visualizes the extensibility of individual bonds, which is different from the overall extensibility of a flexible polymer chain. Therefore, controlling and visualizing bond extensibility in new kinds of polymer systems would be interesting. To explore this, we use optical stepper lithography to produce a wide variety of PLMs, including structures that have not yet been synthesized through other bottom-up methods. Moreover, we show that changing the designed shapes of sub-tile features in LMs provides a means of controlling the degree of extensibility of bonds within colloidal linkages. Our experimental advances in lithographic preassembly, real-space visualization using optical microscopy, and lock-and-key particle tracking reveal distinct longitudinal fluctuations related to bond extensibility as a consequence of only equilibrium Brownian excitations.

RESULTS

Design and fabrication of PLMs

We design and fabricate a wide variety of self-integral polylithomeric linkage systems by extending litho-PAMs (*20*), which until now has only been used to create preconfigured 2D systems of unlinked mobile colloidal tiles confined by an outer wall. Using a quartz-chrome lithographic mask (150 mm by 150 mm; Digidat Inc.), we use optical stepper lithography to manufacture microscale lock-and-key PLMs, which we have digitally designed (L-Edit, Tanner Research). Because the minimum trench feature between the head and the tail is 0.8 μm, imposed by the type of photoresist and the diffraction limit of the stepper [ASML stepper, PAS 5500/200, 5× reduction, ultraviolet (UV) i-line of 365 nm, ≈250 nm minimum feature size], the overall dimensions of individual LMs are near the upper limit of the colloidal scale (≈10 μm).

Individual LMs are designed to have a variety of shapes; PLMs can be made of one or more types (i.e., shapes) of LMs. A simple PLM chain can be made of just a single LM shape [see, e.g., the normal cavity (NC)–type LM in Fig. 1A, top]: a convex rounded-rectangular head, a slender rectangular neck, and a tail having a rounded-rectangular internal concave cavity into which the head of a neighboring LM can also be printed (see Materials and Methods for exact dimensions of subparticle features). We customize the flexibility of junctions by adjusting the designed parameters of the head, tail, cavity, and neck; for instance, the cavity can be enlarged somewhat [see the large cavity (LC)–type LM in Fig. 1A, bottom]. More complex PLMs are made using two or more different LM shapes and appropriate junctions. We then copy, translate, rotate, and, if necessary, mutate shapes of LMs to form PLMs that mimic and go beyond classic molecular polymer architectures. We have made a porous quasi-2D honeycomb mesh that represents systems with a high level of coupling (Fig. 1B), a dendrimer with several hierarchical levels of branching (Fig. 1C), a spiral with flexible bridges (Fig. 1D), and branched polymers (Fig. 1E). On an individual glass wafer (100 mm in diameter, 500 μm in thickness), we print 16 different regions, each containing several PLMs, in a 4 × 4 array. Printed PLMs can be individually released using a release solution-dispersion (RSD) containing a depletion agent that inhibits lift-off of LMs, and the evolution of a PLM's conformation is then recorded as an image sequence and later analyzed. Additional details associated with design, fabrication, release, and imaging are provided in Materials and Methods.

Real-time visualization of release and fluctuation

We demonstrate the versatility of our lithographic method for making free-standing polymer-like colloidal chain structures having a wide variety of preassembled dimensions, topologies, configurations, and intrinsic local curvatures. We have successfully produced and released a four-arm star (movie S1), branched polymers (Fig. 2, A and B, and movie S2) and bridged spiral polymers with varying intrinsic curvature (Fig. 2, C and D, and movie S3), dendrimers with multiple branching levels (Fig. 2, E and F, and movie S4), and quasi-2D mesh particles (Fig. 2, G and H, and movie S5). In Fig. 2, we display grayscale optical micrographs of PLMs and zoomed-in insets, both before and long after release (≈30 hours). By performing time-lapse high-resolution video optical microscopy, we record movies of the collective dynamics of these colloidal linkages that reveal positions and orientations of all individual LMs. Our experiments effectively provide real-space visualization of entropically excited conformations of many analogs of molecular polymers, yielding submonomer resolution of the positions and orientations of all constituent LMs.

Particle tracking and statistical properties

To go beyond a qualitative description of dynamics and fluctuations, we have advanced and refined an image analysis and particle tracking

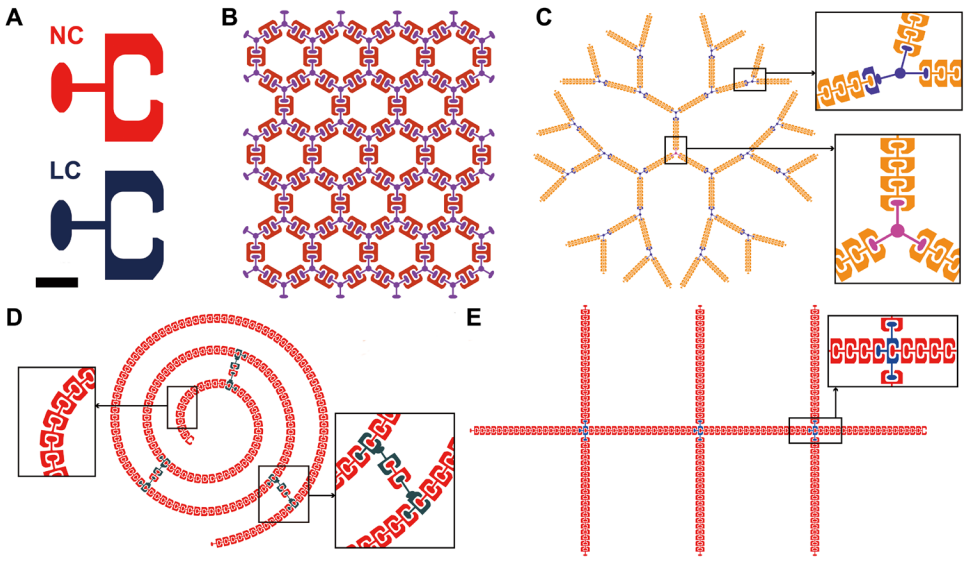

Fig. 1. Designs of lithographic monomers (LMs) and sterically bonded lock-and-key PLMs. (**A**) Basic LMs designed to have convex heads and tails with concave cavities: normal cavity (NC; red, top); larger cavity (LC, dark blue, bottom). Internal cavity lengths are 4.5 μm for NC and 5.0 μm for LC. Scale bar, 5 μm (wafer scale). (**B**) Quasi-2D honeycomb mesh PLM composed of di-cavity LMs (dark red) and tri-head LMs (purple). (**C**) 3-2-2-2 dendrimer PLM. Insets: Mono-cavity, di-head branched LM (blue, top box), and tri-head LM (magenta, bottom box). (**D**) Three-bridged chiral(−) spiral PLM. The LMs here have intrinsic curvatures that vary along the spiral. Insets: LMs designed to have nonzero intrinsic curvature (left box); Cross-linking LMs (right box). (**E**) Symmetric branched PLM having three pairs of symmetric side chains off a central backbone. Inset (box, arrow): Detail showing multiheaded branching LM (blue) at a branching point.

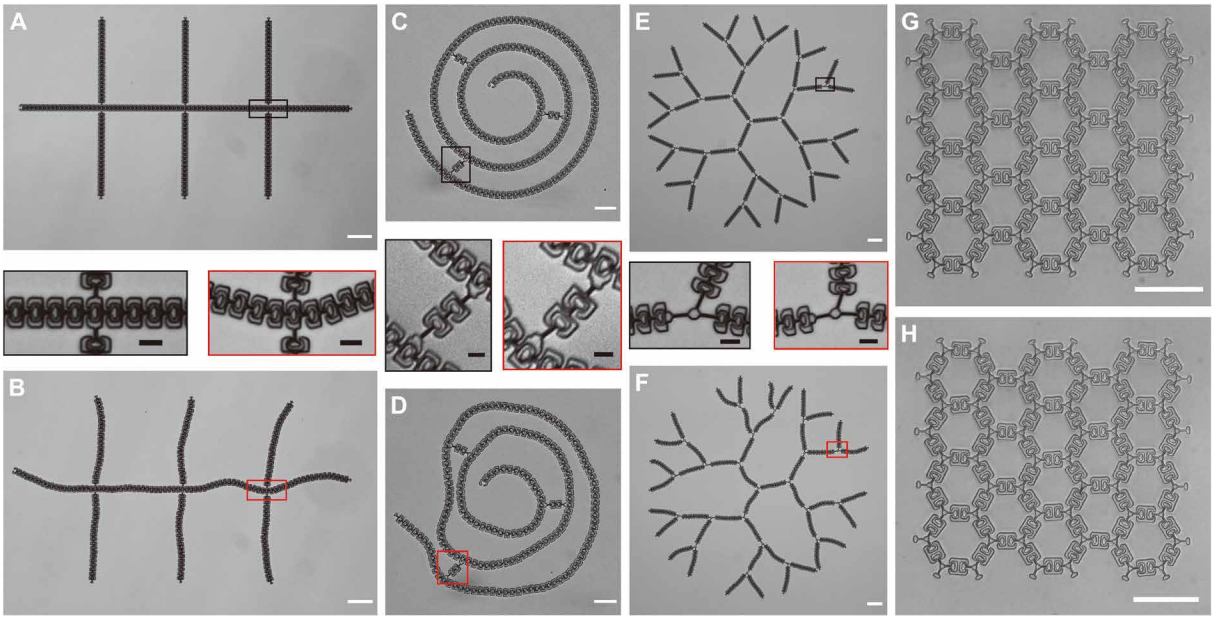

Fig. 2. Pre- and post-release transmission bright-field microscopy images of fabricated PLMs immersed in a RSD. Symmetric branched PLM: (**A**) before release and (**B**) 30 hours after release. Three-bridged chiral(−) spiral PLM: (**C**) before and (**D**) 30 hours after release. 3-2-2-2 Dendrimer PLM: (**E**) before and (**F**) 30 hours after release. Quasi-2D honeycomb mesh PLM: (**G**) before and (**H**) 30 hours after release. Corresponding zoomed images [between parts (A) and (B), (C) and (D), and (E) and (F)] show branching points: prerelease (black boxes) and postrelease (red boxes). Brownian excitations cause fluctuations in conformations of postrelease PLMs. Scale bars, 50 μm (white) and 10 μm (black).

method, which works for complex lock-and-key shapes in close proximity, to determine the positional and angular coordinates of each individual NC-type LM (Fig. 3, A to C). Using these coordinates, we then calculate inter-LM spacings, l, and inter-LM angles, α, between adjacent LMs. This method provides an accuracy within ≈0.5% for inter-LM spacing and ≈0.2 deg for inter-LM angles using a preconfigured chain with known parameters before releasing as a reference. To obtain an approximate sampling of independent

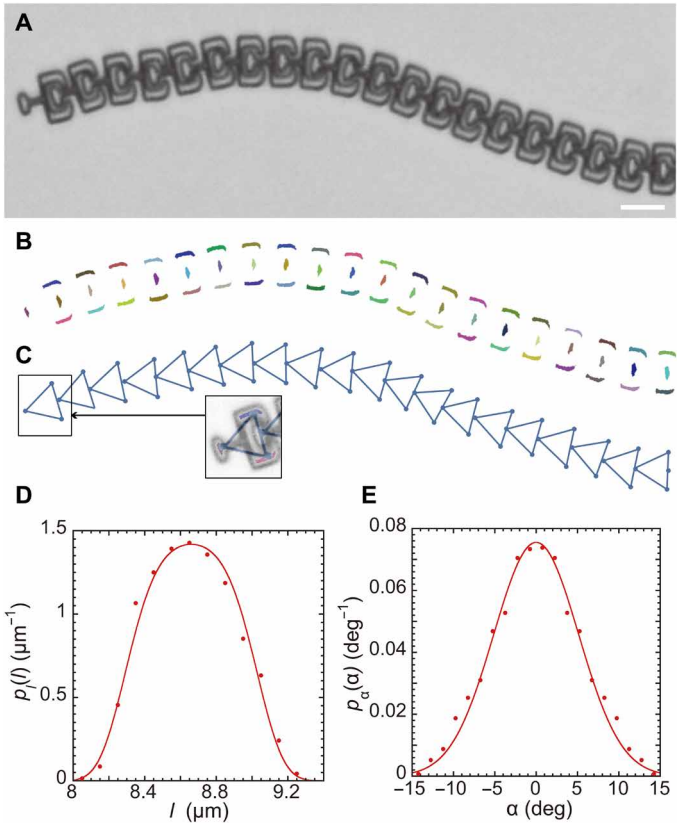

Fig. 3. Particle tracking and statistical properties of linear chains of LMs obtained from arms of branched PLMs. (**A**) Transmission micrograph of an arm of NC-type LMs (grayscale from RGB color). Scale bar, 10 μm. (**B**) Extracted morphological components of (A), yielding head and tail subparticle features (colored regions). Each head produces one colored region; each tail produces two colored regions, one on each side of the cavity. (**C**) Triangles represent extracted positions and orientations of LMs from centroids of morphological components in (B). Inset: Overlay of (A) to (C) onto one monomer. (**D**) Observed probability density of interparticle (i.e., inter-LM) centroid spacing, *l*, defined as the distance between the centers of two adjacent triangles, of NC-type PLMs (PLM_{NC}s) irrespective of the inter-LM bond angle α. Fit: Quartic potential in a Boltzmann distribution [line, see text, coefficient of determination (R^2) = 0.98]. (**E**) Observed probability density of α, defined by the relative orientation between two adjacent triangles of PLM_{NC}s, assuming even symmetry about α = 0 and irrespective of *l*. Fit: Quadratic potential in a Boltzmann distribution, yielding a Gaussian function (line, see text, R^2 = 0.98). deg = °.

members of an equilibrium ensemble of Brownian conformations after release, we analyze images separated by many frames (i.e., ≈500 frames, ≈2 hours).

Using this ensemble, we calculate the statistics of polymeric properties such as the normalized probability density functions of inter-LM spacing, $p_l(l)$ (Fig. 3D), and inter-LM angle, $p_\alpha(\alpha)$ (Fig. 3E). The shapes of the observed peaks for $p_l(l)$ and $p_\alpha(\alpha)$ are substantially different. The peak for $p_l(l)$ in Fig. 3D is obviously non-Gaussian and has a flattened top, whereas the observed peak for $p_\alpha(\alpha)$ in Fig. 3E is nearly Gaussian. Therefore, we attempt to fit $p_l(l)$ and $p_\alpha(\alpha)$ to Boltzmann distributions that assume quartic and quadratic potential energies, respectively. These fits well describe the measured distributions [see lines in Fig. 3 (D and E), respectively]; the quartic term is essential for capturing the non-Gaussian nature of $p_l(l)$. Correspondingly, in Fig. 4 (A and B), we display the measured potential for inter-LM spacing, $U_l(l)$, and angle, $U_\alpha(\alpha)$, extracted from Fig. 3 (D and E), respectively, assuming Boltzmann statistics (NC-type LMs: red points), and we also show the fits to these extracted potential energies (NC-type LMs: red lines).

Comparison between PLMs with different cavities

To demonstrate that we can design and fabricate PLMs having different types of steric lock-and-key bonds that yield different resulting properties and behavior, we compare the potentials, persistence lengths, and extensibilities of linear PLM segments made using two differently designed LMs, one with an NC (NC-type, LM_{NC}) and the other with a larger cavity (LC-type, LM_{LC}).

First, we co-plot the potentials related to inter-LM spacing for both types of PLMs (Fig. 4A). We fit the potential associated with inter-LM spacing with $U_l(l) = U_{l2}[(l/l_0) - 1]^2 + U_{l4}[(l/l_0) - 1]^4$, where l_0 represents the most probable spacing and U_{l2} and U_{l4} represent potential coefficient values related to quadratic and quartic terms, respectively; each type of LM can have different values of l_0, U_{l2}, and U_{l4}. After performing the fitting, we find that in the immediate vicinity of l_0 ($l_{0,NC}$ = 8.674 ± 0.004 μm, $l_{0,LC}$ = 8.629 ± 0.005 μm), where the second-order term (U_{l2}) dominates, both fitted U_{l2} parameters are similar [$U_{l2,NC}/(k_BT)$ = 187 ± 57 and $U_{l2,LC}/(k_BT)$ = 143 ± 27]. However, for values of *l* that are further away from l_0, the quartic term dominates, and we find a large difference in the associated fit parameters: $U_{l4,NC}/(k_BT) = (1.39 \pm 0.14) \times 10^5$ and $U_{l4,LC}/(k_BT) = (2.66 \pm 0.36) \times 10^4$ such that $U_{l4,NC} > U_{l4,LC}$, which is consistent with the smaller designed cavity of the NC-type LM as compared to the LC-type LM. All observed values of *l* are within the geometrical limits implied by the designed lock-and-key features for both types of rigid LMs (7.5 μm < l_{NC} < 9.5 μm, 7.2 μm < l_{LC} < 9.7 μm). This, along with hard in-plane interactions between head and tail-cavity features in these rigid LMs, implies incompressibility and inextensibility of inter-LM bonds beyond these ranges.

Next, for each type of LM, we fit the measured potential as a function of inter-LM angle, $U_\alpha(\alpha)$, in Fig. 4B to $U_\alpha(\alpha) = U_{\alpha 2}\,\alpha^2$, where $U_{\alpha 2}$ represents a potential coefficient value related to this quadratic form. The observed $U_\alpha(\alpha)$ of NC-type and LC-type PLMs can both be captured well by the same quadratic form, and the $U_{\alpha 2}$ fit parameters are also distinguishably different: $U_{\alpha 2,NC}/(k_BT\ \mathrm{deg}^{-2})$ = 0.0190 ± 0.0008 and $U_{\alpha 2,LC}/(k_BT\ \mathrm{deg}^{-2})$ = 0.0146 ± 0.0003. All observed values of α are also within the designed limits ($|\alpha_{NC}| < 24.5°$ and $|\alpha_{LC}| < 26.5°$) for both types of rigid LMs.

In addition, we calculate $\langle\cos(\theta(L))\rangle$, where $\theta(L)$ represents an angle between a first LM and a second LM that is *N* particles away, such that $L = Nl_0$, and averaging over the ensemble is performed (Fig. 4C). By fitting to a decaying exponential function, $\langle\cos(\theta(L))\rangle = \exp.(-L/L_p)$, we find that the resulting persistence lengths for NC-LMs and LC-LMs are nearly the same given one SD uncertainties: $L_{p,NC} = (267 \pm 5)\ l_{0,NC}$ and $L_{p,LC} = (250 \pm 12)\ l_{0,LC}$. This is consistent with the very similar potentials in angle for these two types in Fig. 4B.

We have also measured the extensibilities of both NC-type and LC-type steric lock-and-key bonds, and through analysis, we show that these different designs lead to markedly different extensibilities. Here, the bond extensibility, an intrinsic property between two adjacent LMs related to their shapes, is differently defined than classic extensibility of molecular polymers. We quantify the extensibility between adjacent LMs by making histograms of contour length for different *N* between the centroids of an *i*-th LM and (*i* + *N*)-th LM in the same linear chain, where the index *i* is varied to cover the

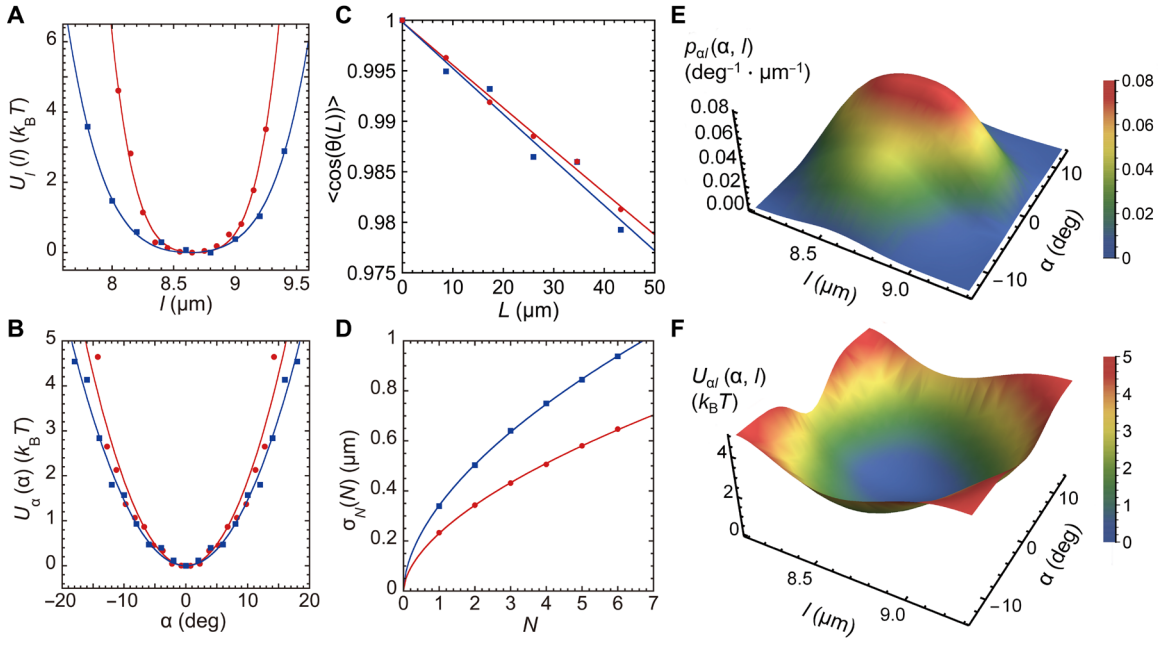

Fig. 4. Equilibrium bond characteristics of PLM_{NC}s and PLM_{LC}s: Designer bond extensibility and semiflexibility. (**A**) Extracted potential of interparticle centroid spacing, $U_l(l)$, between adjacent LMs, assuming Boltzmann statistics, irrespective of bond angle α: PLM_{NC} (red circles) and PLM_{LC} (blue squares). Solid lines: fits to quartic potentials for NC-type (red, $R^2 = 0.993$) and LC-type (blue, $R^2 = 0.998$). Fitted most probable spacing l_0 between LMs for both NC and LC types of PLMs are nearly the same: $l_0 \approx 8.65$ μm. (**B**) Extracted potential of bond angle, $U_\alpha(\alpha)$, assuming Boltzmann statistics and U_α even in α, irrespective of l. Solid lines: Fits to quadratic potentials for NC-type (red, $R^2 = 0.94$) and LC-type (blue, $R^2 = 0.98$). (**C**) Persistence length L_p is obtained by fitting observations of <cos(θ)> [symbols same as in (A)] as a function of length along the contour, L, to $\exp(-L/L_p)$: NC-type (red line, $R^2 = 0.994$); LC-type (blue line, $R^2 = 0.966$). (**D**) SD σ_N of spacing between N LMs along a PLM chain [symbols same as in (A)]. Fits to power law functions: NC-type (red line, $R^2 = 0.9997$); LC-type (blue line, $R^2 = 0.9998$). Surface plots for PLM_{NC}s: (**E**) 2D probability density function, $p_{\alpha l}(\alpha,l)$, assuming even symmetry for α, and (**F**) extracted 2D inter-LM potential $U_{\alpha l}(\alpha,l)$ from (E) assuming Boltzmann statistics.

chain. We find that the average contour length $<L(N)>$ is simply linear and nearly identical for both NC-type and LC-type PLMs; this is consistent with their overall designed lengths, which are the same. Using these histograms at each N, we also calculate the SD of contour length (i.e., spacing), σ_N. If all constituent LMs in a PLM chain would be statistically independent, under Brownian excitations, then we would expect σ_N to be proportional to the square root of N. However, different cavity sizes of LMs offer different accessible microstates for NC- and LC-type PLMs, so $\sigma_{N,NC}$ and $\sigma_{N,LC}$ (i.e., widths of their respective distributions of contour length) are noticeably different. We have tried fitting these σ_N to square root of N behavior, but the quality of fit is not nearly as good as a fit with a power law of the form $\sigma_N = aN^b$ (Fig. 4D). The power law exponents controlling the growth in σ_N are similar ($b_{NC} = 0.564 \pm 0.005$, $b_{LC} = 0.574 \pm 0.006$); yet, the overall magnitudes are quite different ($a_{NC} = 0.230 \pm 0.002$ μm, $a_{LC} = 0.342 \pm 0.002$ μm), consistent with the larger cavity design and greater extensibility of the LC-type bond as compared to the NC-type bond.

By making a discrete 2D histogram of the observed inter-LM probability as a function of l and α assuming even behavior in α and fitting it using a 2D cubic spline function, we obtain a smoothed surface plot of normalized probability density $p_{\alpha l}(\alpha,l)$ for bonds between NC-type LMs obtained via particle tracking (Fig. 4E). Similarly, we also display the corresponding smoothed potential surface $U_{\alpha l}(\alpha,l)$ for NC-type bonds (Fig. 4F) obtained from the Boltzmann factor using this probability density. Our measurements indicate that there is a nearly flat region in $U_{\alpha l}$ along the l axis that reflects the broad anharmonic well in Fig. 4A. This 2D surface potential also provides a more complete picture of the limits of the NC-type lock-and-key junction's allowed internal degrees of freedom than the simplified 1D projections in Fig. 4 (A and B).

Evolution from out-of-equilibrium conformations

By preconfiguring NC-type LMs having inter-LM bonds with zero intrinsic curvature into an open ring-like initial PLM conformation and releasing this far-from-equilibrium PLM, we show that the curvature distribution evolves through Brownian excitations toward equilibrium. To obtain local curvature as a function of contour length and distributions of local curvature, we skeletonize the observed contour associated with the centers of the LMs within the evolving PLM (Fig. 5, A to F). We calculate the local curvature and colorize the backbone skeleton accordingly to encode positive (blue) and negative (red) curvature (see Materials and Methods). The single curvature of the preconfigured PLM before release is reflected initially by a delta function (red arrow) in the distribution, and this peak rapidly spreads out during a short period of time associated with partial release (i.e., from ≈2.4 to ≈2.6 hours) (Fig. 5G).

After 24 hours, there is a higher percentage of gray (i.e., nearly zero curvature) along the chain, as well as some small regions of red (i.e., negative curvature). After 72 hours, even longer gray regions of nearly zero curvature can be seen (Fig. 5F). Also, curvature appears to become concentrated in a few local regions along the chain; these are separated by mostly straight regions. Because the overall size of this PLM chain exceeds the colloidal scale, its evolution toward the equilibrium conformation of a completely straight chain is very slow, and the time scale for Brownian excitations to straighten out

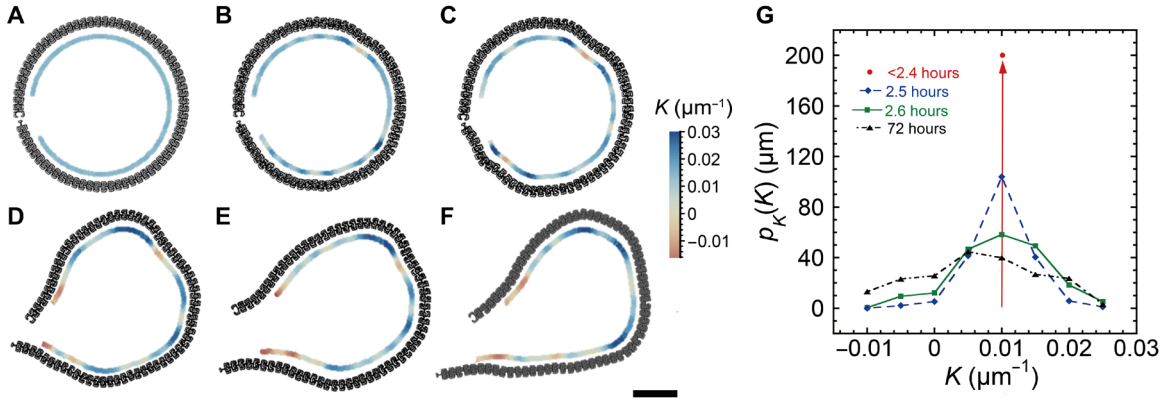

Fig. 5. Temporal evolution of local curvature in a linear PLM_{NC} after release in a far-from-equilibrium initial conformation. Designed intrinsic bond curvature is zero: 71 straight-neck NC-type LMs have initial relative orientations of 5° between two adjacent LMs. Grayscale images show evolving PLM conformations at different times after adding the RSD: (**A**) before onset of release: 0 to 2.4 hours; (**B**) partial release: 2.5 hours; (**C**) just after total release: 2.6 hours, (**D**) 11 hours, (**E**) 24 hours, and (**F**) 72 hours. Scale bar, (A to F): 50 μm. Inner colored lines in (A) to (F): Corresponding calculated curvatures *K* (see text, color scale at right). (**G**) Probability density of curvature, $p_K(K)$, for different times after adding the RSD (see inset legend). The prerelease distribution of curvature is spike-like for 0 to 2.4 hours; after complete release, the distribution of curvature becomes distributied over a wider range of *K* as the system evolves slowly toward $\langle K \rangle = 0$.

the remaining localized regions of higher curvature is longer than our observation time (216 hours).

DISCUSSION

We have designed and lithographically fabricated PLMs as dynamically interesting and readily visualizable colloidal mimics of a wide variety of polymers, wherein constituent LMs are connected by steric lock-and-key linkages without any need for programmable complex attractive interactions through patchy molecular functionalization of particle surfaces. Beyond existing synthetic molecular polymer structures, such as highly branched polymers and dendrimers, our top-down approach has enabled us to access new types of polymer structures, such as a cross-linked chiral spiral, that have not been previously synthesized in either molecular or colloidal form to the best of our knowledge. Thus, without inducing in-plane attractions between lithographic particles and instead by preconfiguring steric lock-and-key shapes with effectively hard in-plane interactions, we have shown that litho-PAMs is not limited only to densely patterned nonsterically interlocking particles, such as a quasi-crystal of Penrose kites and darts, that otherwise melt and lose memory of their initial configurations if external confining walls are removed. From a micromechanical point of view, PLMs are effectively mobile colloidal linkages that fluctuate and exhibit a superposition of damped transverse and longitudinal wave-like motions as a consequence of LM coupling in the presence of broadband Brownian excitations.

To obtain such a wide variety of PLM structures, we have designed different subparticle features into LMs, conferring different types of LMs that can have shape-controlled steric bonding characteristics. These subparticle features are reminiscent of secondary structures of folded proteins. For example, cross-linking LMs at branching points can give rise to LMs having multiple heads and/or multiple tails, rather than the most basic and prevalent single head-tail LM design. As an illustration of this, the fluctuating 2D mesh (Fig. 2H) is composed of three-head LMs and two-tail LMs. Also, even regarding the single head-tail LM design, we have varied the angle between the head and the tail through the connecting neck, thereby imposing a lithographically predesigned intrinsic curvature, which can be spatially varied, into linear chains of LMs, as we have shown with the cross-linked chiral spiral. Beyond this, by controlling the size of the cavity in the tail of single head-tail LMs, as we have demonstrated through particle tracking microscopy experiments after release, even relatively small differences in the cavity lengths can result in readily measurable differences in the extensibilities of PLMs composed of NC-type and LC-type LMs. Thus, the lithographic design and preassembly of shapes of LMs can be used to control the nature of inter-LM bonding, including aspects of multivalency, chirality, extensibility, flexibility, and intrinsic curvature. This degree of control goes well beyond the topology and overall structures of different types of PLMs, which could be extended to include self-similar "fractal" polymers.

Our experiments involving NC-type and LC-type PLMs show that PLMs offer access to an interesting and unusual range of polymer structures that have extensible bonds that can be controlled by top-down design. The nearly hard interactions between the head of one LM and the cavity of an adjacently bonded LM lead to a flattened, dominantly quartic, rather than quadratic, inter-LM potential associated with longitudinal extension and compression. Whereas molecular polymer systems have covalent bonds between atoms that are effectively inextensible, even larger extensibility in inter-LM bonds within PLMs could be programmed through the design of even longer cavity features in constituent LMs. Thus, through PLMs, it is possible to make and study polymers that are semiflexible yet have substantial extensibility; this is especially interesting in 2D systems for which Brownian excitations between noninterlocking particles at high densities are known to give rise to long-wavelength Mermin-Wagner fluctuations. In general, the influence that extensible steric lock-and-key bonds can have on Kosterlitz-Thouless phenomena (*25*) and Goldstone modes (*26*) in dense 2D Brownian systems of mobile tiles remains intriguing, and our approach now makes these systems accessible.

Beyond equilibrium fluctuations, our example of the evolution of local curvature in a ring-like initial PLM conformation of lock-and-key LMs, which are all connected by steric bonds that have zero intrinsic curvature, highlights the potential for making and studying the behavior of local entropy flux [i.e., caliber (*27*, *28*)] in

far-from-equilibrium systems. Because the best forms of modern stepper lithography can achieve minimum feature sizes more than an order of magnitude below the limit of the 5× reduction Hg i-line optical stepper that we have used, we anticipate that it will be possible to construct systems that are composed of much smaller LMs and therefore have much more rapid temporal evolution under Brownian excitations. Moreover, we also anticipate that linear and nonlinear responses of individual PLMs to externally applied fields, particularly flow fields and electromagnetic fields, will be interesting to study.

While the conceptual development and experimental demonstrations of PLMs here represent major advances in interconnected dynamic systems of mobile linkages that are small enough for entropic effects (i.e., Brownian excitations) to be important, as they are for molecular polymers, there are some limitations in the current examples that future work could potentially overcome. Reducing the persistence length and approaching the limit of flexible polymers could potentially be achieved through differently designed LMs and their interconnections. Other nanolithography techniques, not just optical stepper lithography, could be used to make PLMs, and these could be used to reduce the sizes of LMs and the overall PLMs to speed up conformational dynamics resulting from Brownian excitations. For these smaller PLMs, using simple bright-field microscopy would not necessarily yield high quality tracking information about subparticle features; so, measuring dynamics using a real-time or high-speed visualization method that offers higher spatial resolution would likely also be necessary. The visualization of these smaller PLMs to sub-LM detail could involve the use of fluorophores or other molecular markers in the composition of the LMs, and it might involve alternative techniques such as dark-field, super-resolution, or scanning probe microscopies.

We expect that our findings will spark new efforts in several different directions. Theories and simulations of polymer dynamics will need to be extended to treat anharmonic extensible inter-LM steric bonds. Related to this, longer wavelength longitudinal modes of motion are readily observable in the systems of semiflexible PLMs that we have already generated, and these need further theoretical statistical characterizations. Different head and cavity designs would enable a more thorough exploration of the dynamics of extensible polymers, both in experiments and in theory. Interactions between locally proximate PLMs would also be possible and interesting to study. Confinement of PLMs within certain shapes of rigid confining walls could also be accomplished to see how this confinement influences conformations. Tuning in-plane interactions between the surfaces of LMs to be other than hard, for instance, through size and concentration of other depletion agents, would also be possible and could substantially influence the inter-LM potentials. Overall, the future is bright in regard to expanding the variety and scope of experimentally realizable colloidal mimics of molecular polymer systems and polymer dynamics based on the approaches here.

MATERIALS AND METHODS

Designing LM shapes and initial conformations of PLMs

Simple mono-head, mono-tail LMs (see Fig. 1A) are designed to have a convex rounded-rectangular head (6.0 μm in width and 2.5 μm in length), a slender rectangular neck (1.0 μm in width and 4.0 μm in length), and a tail (outer width: 13.0 μm; outer length: 7.0 μm) having a rounded-rectangular internal concave cavity with an opening (inner width: 8.0 μm; inner length: 4.5 μm for NC-type and 5.0 μm for LC-type). To create a design of a chain-like PLM, the head of a given LM is positioned inside the internal cavity of the tail of a neighboring LM, and this is repeated as additional LMs are added. To design various 1D, quasi-2D, and 2D PLM patterns, we not only copy and translate standard LMs but also mutate, fuse, or modify their shapes, particularly at junctions and nodes. For example, the 2D mesh (Fig. 1B) is composed of two differently shaped LMs that result from (i) the fusion of three heads with necks into an equilateral tri-star shape and (ii) the fusion of two tails with cavities. Alternatively, the junctions in polylithomeric dendrimers are made of one tail and the fusion of three heads with necks (Fig. 1C). Through a different type of modification, the spiral's intrinsic curvature has been designed to change from 0.014 μm^{-1} (interior terminal end) to 0.0046 μm^{-1} (exterior terminal end), primarily by continuously varying the angle between necks and tails and by mutating the tail structure including the cavity. A wide variety of branched PLMs can be designed by varying the structures of junction LMs, which can have controllable numbers of bonds, bond lengths, and bond angles; as an example, we fuse an extra head with a neck onto a tail (Fig. 1D). As another example, the junctions of the branched polymer are created by fusing two additional side heads onto the tail of a standard NC-type LM (Fig. 1E).

Fabrication by photolithography

To facilitate imaging and ensure a negatively charged, flat, smooth substrate below the fabricated PLMs, we use a transparent glass wafer (University Wafer, polished borosilicate 33; 500 μm thick, 100 mm in diameter, prime). After prebaking this wafer at 200 °C for 3 min and cooling back to 25 °C on aluminum foil to remove any adsorbed moisture, we spin-coat [500 rpm for 5 s with acceleration of 100 rpm s^{-1} and then 3000 rpm for 30 s with acceleration of 300 rpm s^{-1} (Headway Research, PWM32 Spin Coater)] a release layer of OmniCoat (MicroChem Inc.) onto the glass wafer. After baking at 200 °C for 1 min, the OmniCoat forms a solid transparent thin (≈15 nm) release layer. The wafer is then cooled to 25 °C. We spin-coat and bake this OmniCoat layer a second time using the same procedure to ensure that the entire wafer is fully coated and thereby achieve complete particle release. Onto the layer of OmniCoat, we spin-coat a layer of epoxy SU-8-2002 (MicroChem Inc.) negative photoresist and subsequently bake at 95 °C for 90 s. A solid, transparent, ≈2-μm-thick layer of uncross-linked SU-8 is formed, and the wafer is cooled to 25 °C. This coated wafer is then loaded into the stepper and exposed using the quartz-chrome mask to patterned UV light (energy dose of 140 mJ cm^{-2}), which selectively cross-links the SU-8 photoresist into the desired preconfigured PLMs on the wafer. After postexposure baking at 95 °C for 75 s and cooling to 25°C, any remaining unexposed and uncross-linked SU-8 is removed by SU-8 Developer (MicroChem Inc., 1-methoxy-2-propyl acetate) for 3 min through continuous agitation. Next, we rinse the wafer in isopropyl alcohol and dry it with a flow of nitrogen gas to remove any residual uncross-linked SU-8, yielding disconnected, transparent preassembled PLMs attached to the release layer of OmniCoat.

Release and imaging of PLMs

Before releasing, we first build an elastomeric polydimethylsiloxane (PDMS) well, which confines the RSD within a certain volume. We first mix a PDMS elastomer and its curing agent (SYLGARD 184) at a weight ratio of 10:1 on a clean petri dish, leave it at 25°C for degassing overnight, and put it in a vacuum oven at 80°C for 2 hours. Then,

we cut this disk-like layer of PDMS into a square-frame well that is about 3 mm high and has a 1.3-cm outer edge length and a 1-cm inner edge length. Next, we clean the region around the selected PLM on the glass wafer with deionized water using a cotton-tipped applicator, thereby removing OmniCoat, carefully attach the PDMS well onto this region, and bake at 80 °C for 2 hours to form a water-impermeable bond with the glass surface.

The composition of the RSD is vital not only to gradually dissolve the OmniCoat release layer but also to keep the released PLMs stable against aggregation and close to the surface of the glass wafer. Therefore, besides tetramethylammonium hydroxide [0.5% (w/v); Sigma-Aldrich] as a basic release agent that dissolves OmniCoat, we also include SDS (25 mM; MP Biomedicals, ultrapure) as a stabilizing agent, and polystyrene spheres [carboxylate-stabilized, surfactant-free; MagSphere; 52 nm in diameter, 1.5% (w/v) solids] as a depletion agent that strongly inhibits the lower faces of all released LM particles from leaving the vicinity of the plane. Gravitational forces normal to the plane, caused by the density difference between the cross-linked SU-8 and the RSD, also act in concert with the depletion forces to provide additional stabilization of the PLMs against breakup over long times after release by further suppressing out-of-plane motion of constituent LMs. A highly screened short-range charge repulsion, provided by negative charges on the glass wafer and on the surfaces of the SU-8 particles (via adsorbed dodecyl sulfate anions), ensures lubrication and mobility of all particles after release. Because the RSD when first made may contain some small aggregates, we filter the RSD using a 2.5-μm filter, centrifuge it in a 1.5-ml conical tube at 500 rpm for 4 min, and withdraw all but the lowest ≈50 μl. We completely fill the PDMS well with this RSD and immediately put a coverslip over it to reduce evaporation.

We place the wafer with RSD-filled PDMS well onto an inverted optical microscope (Nikon TE2000, 10× or 20× CFI plan achromat objectives, Nikon Z7 and D5300 cameras, silent mode). Bright-field transmission images, taken through the wafer, are recorded every 15 s using Camera Control Pro software (Nikon), yielding in situ high-resolution time-lapse movies of fluctuating Brownian PLMs.

Image analysis and particle tracking

To analyze these movies, we have gone beyond prior particle tracking routines that merely tracked vertices of polygonal objects (e.g., square tiles or dart tiles) (*20*, *29*). As a first step, we batch process image sequences in Photoshop using built-in functions: grayscale, rotate, crop, 2× image scale, invert, and magic wand to select and remove background via a color range selection/expansion. Using Mathematica (Wolfram Research Inc.), for each LM, we extract a bright region corresponding to each head and two bright regions corresponding to both sides of each tail. We then obtain the centroids of these bright regions to calculate the position and orientation of each LM (routines used: MorphologicalComponents, SelectComponents, and ComponentMeasurements). We also calculate the bond length and bond angles and, assuming a Boltzmann probability, extract an effective bonding potential from the resulting distributions. For the case of steady-state fluctuations of PLMs around an equilibrium conformation, independent members of equilibrium ensembles are approximately obtained by sampling every 500 frames. Each ensemble contains approximately 95 individual LMs. Terminal LMs that are within three monomer units of ends and junctions are excluded from the ensemble, so average bond properties reflect the behavior of monomers within the linear chain.

To calculate the evolution of curvature from a nonequilibrium initial ring-like PLM conformation of LMs that have been designed to have no intrinsic curvature, we first skeletonize the contour of this PLM using Photoshop and Mathematica. We discretize the contour into a set of 400 points and fit these points to circles in groups of 5 points, yielding local curvature that is mapped into color. In this analysis, the ends of the PLM are truncated (by about ≈3 LMs), so the analyzed colored contour is slightly shorter than the actual PLM.

SUPPLEMENTARY MATERIALS

Supplementary material for this article is available at https://science.org/doi/10.1126/sciadv.abg3678

REFERENCES AND NOTES

1. R. J. Young, P. A. Lovell, *Introduction to Polymers* (CRC Press, 2011).
2. A. Hirao, M. Hayashi, S. Loykulnant, K. Sugiyama, S. W. Ryu, N. Haraguchi, A. Matsuo, T. Higashihara, Precise syntheses of chain-multi-functionalized polymers, star-branched polymers, star-linear block polymers, densely branched polymers, and dendritic branched polymers based on iterative approach using functionalized 1,1-diphenylethylene derivatives. *Prog. Polym. Sci.* **30**, 111–182 (2005).
3. S. T. Milner, Polymer brushes. *Science* **251**, 905–914 (1991).
4. P. W. K. Rothemund, Folding DNA to create nanoscale shapes and patterns. *Nature* **440**, 297–302 (2006).
5. Z. Li, Y. Zhang, P. Fullhart, C. A. Mirkin, Reversible and chemically programmable micelle assembly with DNA block-copolymer amphiphiles. *Nano Lett.* **4**, 1055–1058 (2004).
6. K.-F. Arndt, T. Schmidt, R. Reichelt, Thermo-sensitive poly(methyl vinyl ether) micro-gel formed by high energy radiation. *Polymer* **42**, 6785–6791 (2001).
7. P. Li, Z. Chen, M. R. Ryder, C. L. Stern, Q.-H. Guo, X. Wang, O. K. Farha, J. F. Stoddart, Assembly of a porous supramolecular polyknot from rigid trigonal prismatic building blocks. *J. Am. Chem. Soc.* **141**, 12998–13002 (2019).
8. M. T. Nguyen, D. P. Ferris, C. Pezzato, Y. Wang, J. F. Stoddart, Densely charged dodecacationic [3]- and tetracosacationic radial [5]catenanes. *Chem* **4**, 2329–2344 (2018).
9. T. G. Mason, J. Bibette, D. A. Weitz, Relaxation of linear chains of attractive colloidal droplets, in American Physical Society, Annual March Meeting, Los Angeles, CA, 16 to 20 March 1998.
10. R. Dreyfus, J. Baudry, M. L. Roper, M. Fermigier, H. A. Stone, J. Bibette, Microscopic artificial swimmers. *Nature* **437**, 862–865 (2005).
11. K. Zhao, T. G. Mason, Directing colloidal self-assembly through roughness-controlled depletion attractions. *Phys. Rev. Lett.* **99**, 268301 (2007).
12. T. G. Mason, Osmotically driven shape-dependent colloidal separations. *Phys. Rev. E* **66**, 060402 (2002).
13. D. J. Ashton, R. L. Jack, N. B. Wilding, Self-assembly of colloidal polymers via depletion-mediated lock and key binding. *Soft Matter* **9**, 9661–9666 (2013).
14. H.-Y. Chang, C.-W. Huang, Y.-F. Chen, S.-Y. Chen, Y.-J. Sheng, H.-K. Tsao, Assembly of lock-and-key colloids mediated by polymeric depletant. *Langmuir* **31**, 13085–13093 (2015).
15. Y. Wang, Y. Wang, X. Zheng, G.-R. Yi, S. Sacanna, D. J. Pine, M. Weck, Three-dimensional lock and key colloids. *J. Am. Chem. Soc.* **136**, 6866–6869 (2014).
16. C. A. Mirkin, R. L. Letsinger, R. C. Mucic, J. J. Storhoff, A DNA-based method for rationally assembling nanoparticles into macroscopic materials. *Nature* **382**, 607–609 (1996).
17. S.-J. Park, A. A. Lazarides, J. J. Storhoff, L. Pesce, C. A. Mirkin, The structural characterization of oligonucleotide-modified gold nanoparticle networks formed by DNA hybridization. *J. Phys. Chem. B* **108**, 12375–12380 (2004).
18. M. B. Bannwarth, S. Utech, S. Ebert, D. A. Weitz, D. Crespy, K. Landfester, Colloidal polymers with controlled sequence and branching constructed from magnetic field assembled nanoparticles. *ACS Nano* **9**, 2720–2728 (2015).
19. S. Y. Park, A. K. R. Lytton-Jean, B. Lee, S. Weigand, G. C. Schatz, C. A. Mirkin, DNA-programmable nanoparticle crystallization. *Nature* **451**, 553–556 (2008).
20. P.-Y. Wang, T. G. Mason, A Brownian quasi-crystal of pre-assembled colloidal Penrose tiles. *Nature* **561**, 94–99 (2018).
21. S. M. Bhattacharjee, A. Giacometti, A. Maritan, Flory theory for polymers. *J. Phys. Condens. Matter* **25**, 503101 (2013).
22. T. Hugel, M. Grosholz, H. Clausen-Schaumann, A. Pfau, H. Gaub, M. Seitz, Elasticity of single polyelectrolyte chains and their desorption from solid supports studied by AFM based single molecule force spectroscopy. *Macromolecules* **34**, 1039–1047 (2001).
23. X. Liu, G. H. Pollack, Mechanics of F-actin characterized with microfabricated cantilevers. *Biophys. J.* **83**, 2705–2715 (2002).
24. F. Manca, S. Giordano, P. L. Palla, R. Zucca, F. Cleri, L. Colombo, Elasticity of flexible and semiflexible polymers with extensible bonds in the Gibbs and Helmholtz ensembles. *J. Chem. Phys.* **136**, 154906 (2012).

25. K. Zhao, R. Bruinsma, T. G. Mason, Entropic crystal–crystal transitions of Brownian squares. *Proc. Natl. Acad. Sci. U.S.A.* **108**, 2684–2687 (2011).
26. J. Kosterlitz, D. Thouless, Ordering, metastability and phase transitions in two-dimensional systems. *J. Phys. C Solid State Phys.* **6**, 1181–1203 (1973).
27. J. Goldstone, Field theories with « superconductor » solutions. *Nuovo Cim.* **19**, 154–164 (1961).
28. M. J. Hazoglou, V. Walther, P. D. Dixit, K. A. Dill, Communication: Maximum caliber is a general variational principle for nonequilibrium statistical mechanics. *J. Chem. Phys.* **143**, 051104 (2015).
29. E. T. Jaynes, The minimum entropy production principle. *Annu. Rev. Phys. Chem.* **31**, 579–601 (1980).

Acknowledgments: We thank P.-Y. Wang and L. Tokunaga for initial experimental assistance with the stepper lithography. We acknowledge use of the Integrated Systems Nanofabrication Cleanroom at UCLA's California NanoSystems Institute. **Funding:** This work has been partially funded by the National Science Foundation (NSF-DMR-1905347). T.Y. has been partially supported by the China Scholarship Council (CSC) for graduate study and research at UCLA (CSC201806190240). **Author contributions:** Conceptualization: T.G.M. Methodology: T.Y. and T.G.M. Investigation: T.Y. and T.G.M. Software: T.Y. and T.G.M. Formal analysis: T.Y. and T.G.M. Validation: T.Y. and T.G.M. Visualization: T.Y. and T.G.M. Writing (original draft): T.Y. and T.G.M. Writing (review and editing): T.Y. and T.G.M. Supervision: T.G.M. Project administration: T.G.M. **Competing interests:** UCLA's Technology Development Group (TDG) has made an independent decision to file a U.S. patent application based on the approach described here; the authors are required to disclose their results to TDG as a condition of employment. No author has received any compensation related to this filing to date. The authors declare that they have no other competing interests. **Data and materials availability:** All data needed to evaluate the conclusions in the paper are present in the paper and/or the Supplementary Materials.

Submitted 30 December 2020
Accepted 14 July 2021
Published 3 September 2021
10.1126/sciadv.abg3678

Citation: T. Yu, T. G. Mason, Brownian lithographic polymers of steric lock-and-key colloidal linkages. *Sci. Adv.* **7**, eabg3678 (2021).